



CHALMERS
UNIVERSITY OF TECHNOLOGY

Deep Intergranular Fluoride Attack by High Temperature Corrosion on Alloy 625 by LiF in Air at 600°C

Downloaded from: <https://research.chalmers.se>, 2024-11-19 10:25 UTC

Citation for the original published paper (version of record):

Nikbakht, A., Bahramian, B., Geers, C. (2024). Deep Intergranular Fluoride Attack by High Temperature Corrosion on Alloy 625 by LiF in Air at 600°C. *High Temperature Corrosion of Materials*, 101(5): 1055-1066.
<http://dx.doi.org/10.1007/s11085-024-10259-6>

N.B. When citing this work, cite the original published paper.



Deep Intergranular Fluoride Attack by High-Temperature Corrosion on Alloy 625 by LiF in Air at 600 °C

Aida Nikbakht¹ · Behnam Bahramian² · Christine Geers¹

Received: 6 July 2024 / Revised: 8 July 2024 / Accepted: 17 July 2024 /
Published online: 27 July 2024
© The Author(s) 2024

Abstract

In most chemical and high-temperature processes, metals are exposed to temperature gradients which, in turn, affect the extent of corrosion phenomena. In this study, a long, continuous strip of alloy 625 was exposed to lithium fluoride in a temperature range of 50–600 °C, air environment. The hottest section of this strip was analyzed as a coupon and compared with two other coupons which were exposed isothermally. One of the isothermal exposures was carried out in a tube furnace, and the other one was in a vertical furnace. Oxygen had three different kinds of access to these three coupons, which, in turn, affected the corrosion process. In order to limit the access of oxygen, a long column of lithium fluoride was used in a vertical furnace. The results of the isothermal exposure showed that more access of oxygen in a horizontal tube furnace facilitated the fluoride ingress to a great extent. However, a long sample exposed to a temperature gradient suffered more corrosion attack than the isothermal coupon, under the same LiF load in the vertical furnace. This was associated with the reduction of oxygen at a larger cathode area reaching into colder regions in Inconel 625 strip. Increased oxygen reduction also increases the efficiency of an inner anode at the hottest section, causing the observed rapid intergranular fluoride uptake. The study proposes a mechanism explaining these observations.

Keywords Alkali fluorides · Intergranular corrosion · Inconel 625 · Temperature gradient · Inner anode · High temperature corrosion

✉ Aida Nikbakht
nikbakht@chalmers.se

¹ Department of Chemistry and Chemical Engineering, Chalmers University of Technology, 41296 Gothenburg, Sweden

² Rechargeable Battery Materials, Umicore, 2250 Olen, Belgium

Introduction

Accelerated oxidation in the presence of alkali halogenides has been a long-standing research topic. The most known combinations are alkali chlorides in waste-to-energy combustion environments [1]. Alkali fluorides, on the other hand, have been mostly investigated in context to thermal storage technologies [1–4]. Molten salt technology in general is applicable in a variety of areas such as heat transfer, thermal energy storage, batteries and fuel cells [5]. Molten fluoride salts have been proposed for use as a carrier of nuclear fuels and coolants because of their low vapor pressure, high boiling point, good thermal conductivity and relatively good chemical inertness [6]. Molten chlorides, on the other hand, are promising candidates for thermal energy storage, due to their thermal stability and low cost [7]. However, experiments have shown that even cover gases with low amounts of air and humidity levels can cause rapid and uncontrollable corrosion, as observed in a 253MA metal container exposed to a temperature gradient and only condensing chlorides originating from a melt pool [8]. Owing to their relatively low price, molten chlorides have been applied more in industry, and therefore, more research has been carried out on them in this realm. In the studies by Liu et al. in NaCl–CaCl₂–MgCl₂ in the presence of air, Inconel 625 showed better corrosion resistance than Hastelloy X and Hastelloy B-3 at 600 °C [9]. The lower content of Fe in Inconel 625 made it outperform Hastelloy X in this study. In this work, the Cr₂O₃ scale on the surface of Hastelloy X and Inconel 625 was not protective and was destroyed after a short while. However, a relatively dense phase of MgCr₂O₄ was covering the surface which showed protective properties against further attack. There is more data available on chloride salts in comparison with fluorides in general. Also, most of the studies have been done under inert atmosphere, and only few have had air as the environment. It is well known that the purer the environment, the better the alloy performance [10]. However, in the current paper, air is not only an impurity, but the main gas.

This study investigates the corrosion mechanism of Inconel 625 in direct contact with lithium fluoride under filtered air for 168 h and 1000 h in one of the cases. Considering the fact that oxygen plays a prominent role in this type of corrosion, three samples with different configurations in terms of access to oxygen have been studied. Samples presented in this paper have been exposed to 600 °C; however, the effect of temperature gradient was also investigated. The primary aim of this study is to determine how the corrosion process is affected by different levels of access of oxygen through lithium fluoride to the alloy surface. Parallel to this, it was studied if long samples reaching across a wide temperature gradient range behave differently, as long as the part of the strip which was exposed to the same temperature as the isothermal studies is analyzed.

Experimental Procedures

Inconel 625 has been selected for this study. The plate has been hot rolled and heat treated at 1020 °C. The nominal composition of this alloy is found in Table 1. Isothermal studies have been conducted on 15 × 15 × 3 mm³ coupons that have been

Table 1 Nominal alloy compositions (wt%) of the Inconel 625 provided by the supplier

Ni	Cr	Mo	Fe	Nb	Ti	Si	Others
Balance	21.51	8.69	4.32	3.31	0.20	0.12	C 0.02

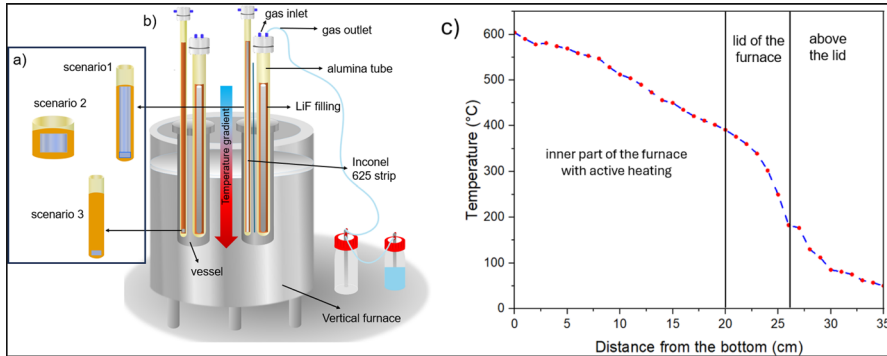


Fig. 1 **a** Configurations of coupons 1, 2 and 3 represented, respectively, by scenarios 1, 2 and 3, **b** vertical furnace used for the gradient study and **c** temperature gradient throughout the long alumina crucible from the bottom to the top zero distance represents the bottom of the crucible which is the hottest part

ground and polished to a 1- μm diamond suspension finish. Thermal gradient studies, on the other hand, were performed on much longer samples, $350 \times 10 \times 3 \text{ mm}^3$ strips, that have been ground up to a 600-grit SiC finish, using a band grinding machine. Coupons and strips have been cut from the same batch of raw material, and filtered air was used as cover gas with a flow rate of $7 \pm 5 \text{ ml/min}$ in both cases. Each scenario has been repeated at least once.

Experimental Setups

Three different scenarios are investigated in this study, and coupons 1, 2 and 3 correspond, respectively, to scenarios 1, 2 and 3. A long thermal gradient sample is vertically placed in a 500-mm-long alumina crucible with an inner diameter of 12 mm (Fig. 1a, scenario 1). This crucible is housed in a steel vessel which is placed in an electric heated modified top loader furnace (model top 60 Nabertherm) (Fig. 1b).

The temperature calibration curve for the long crucibles is shown in Fig. 1c. As labeled in Fig. 1c, three different regimes can be considered for the temperature gradient. From the hottest zone at the bottom of the furnace up to 20 cm, the crucible is in the heated room of the furnace and shows a nearly linear temperature gradient from 400 to 600 $^{\circ}\text{C}$ where the three heating elements are providing active heating. The second range indicates the thick insulated furnace lid constructed of refractory bricks around the vessels. This is where the temperature starts to drop faster. The last part of the curve is where the alumina crucible is reaching out of the modified furnace into air cooling until reaching room temperature. This last part of the gradient ranges from 35 to 183 $^{\circ}\text{C}$ in 10-cm distance difference. For isothermal exposures,

coupon 2 was placed in a small alumina crucible (Fig. 1b, scenario 2) at 600 °C in a horizontal alumina tube furnace. Coupon 3 was also isothermally exposed, but in the vertical setup, with a long column of lithium fluoride on top of it, as shown in Fig. 1b, scenario 3.

The main goal of designing the vertical setup is to achieve a well-defined temperature gradient across the material in contact with LiF temperatures. All samples which are discussed in this paper were exposed to 600 °C in contact with LiF for 168 h, but the exposure with temperature gradient was also extended to 1000 h. Coupon 1 was cut from the Inconel 625 strip which was exposed to a temperature gradient in the vertical setup. The small coupon 2 was fully immersed in LiF in a short alumina crucible in a tube furnace. In the tube furnace, coupons were exposed to a significantly lower amount of salt in comparison with the coupons exposed in the vertical furnace. Coupon 3 was also in full contact with the salt in the vertical setup, with a long stack of LiF on top of it, as shown in Fig. 1a, scenario 3.

What differentiates these scenarios from each other is the environment, meaning that the cathode area is largest in scenario 1, and the flowing cover air has less access to the coupon that lies at the bottom of the alumina tube in scenario 3. In contrast, coupon 2, which is exposed to LiF at the same temperature in the horizontal tube furnace, gets easier in contact with oxygen and salt simultaneously. Indeed, the oxygen can readily permeate through a lower amount of LiF powder in the small crucible.

Characterization of the Samples

In order to characterize the long samples, the strip was cut into $10 \times 3 \times 10 \text{ mm}^3$ pieces, by means of a low-speed saw without coolant. To investigate the cross-sections, the exposed samples were hot mounted into bakelite, as well as the coupon samples. No weight change data are available for the strips in a temperature gradient, since the strips have undergone significant mass loss at each cut. Scanning electron microscope (SEM) analysis and energy-dispersive X-ray spectroscopy (EDX) were done using JEOL JSM-7800F Prime equipped with an EDX detector. The accelerating voltage of the electron beam was set at 15 kV. The K-lines of Li^+ ions are not accessible via EDX analysis; therefore, XRD was utilized to identify diffraction patterns of lithium-containing species. A Bruker D8 Advance powder diffractometer was used for that purpose.

Results

Coupons 1 and 3 were similar in terms of positioning and oxygen access (both were positioned on the bottom of long alumina crucibles with a column of salt on them). However, coupon 1 was part of a long alloy strip, while coupon 3 was a small piece. The shape of oxide scale in coupon 1 is very much defect rich, which makes it less protective in comparison with the compact oxide scale in coupon 3.

As observed in the BSE images in Fig. 2a and d, the oxide scale on coupon 1 was thinner and defect rich. This has led to the base metal being more detectable in the XRD analysis (Fig. 3). Note that the samples were not washed before the XRD analyses to avoid the dissolution of corrosion products. Since more salt had reacted with the alloy surfaces on coupons 2 and 3 which were isothermally exposed, XRD signals of LiF are more pronounced in these samples. The oxide scale in scenario 1 in Fig. 3 exhibits the incorporation of Fe and Cr in addition to Ni. This is in line with the EDX element maps in Fig. 2a, where fluoride has reached underneath the oxide scale and is present deeper in the alloy along grain boundaries in scenario 1. The salt surrounding coupon 1 did not have a yellow color, and Li_2CrO_4 was not detected either in the XRD pattern.

Coupon 2 underwent the most intense fluoride attack of 54 μm deep (Fig. 2b and e). The intergranular attack in this sample is the thickest observed in this study, leading to the detachment of individual grains. This deep intergranular attack is filled with fluoride, which makes the fluoride uptake greater than in scenarios 1 and 3. The oxide scale on this sample is quite heterogeneous, in a way that it rises with very thick nodules up to 18 μm thick at some spots, while it is only 5 μm thick at some other spots. This oxide scale in coupon 2 is very much defect rich as shown in Fig. 2e, not protective, and has not impeded the fluoride ingress during the exposure.

The XRD analysis for coupon 2 (Fig. 3, scenario 2), which was exposed in the horizontal furnace and had continuous access of oxygen, confirms the participation of Cr into the oxide scale. Since Cr has a bigger ionic ratio than Ni, the XRD peaks for $\text{Li}_{0.3}\text{Cr}_{0.05}\text{Ni}_{1.65}\text{O}$ in coupon 1 have been slightly shifted to the right in comparison with $\text{Li}_{0.4}\text{Ni}_{0.6}\text{O}$. The salt surrounding coupon 2 was bright yellow at the salt–alloy interface, which was pointing toward Cr(VI) ions. The XRD pattern in Fig. 3, scenario 2, also confirmed Li_2CrO_4 as an oxide species, which proves the yellow color observed in the salt.

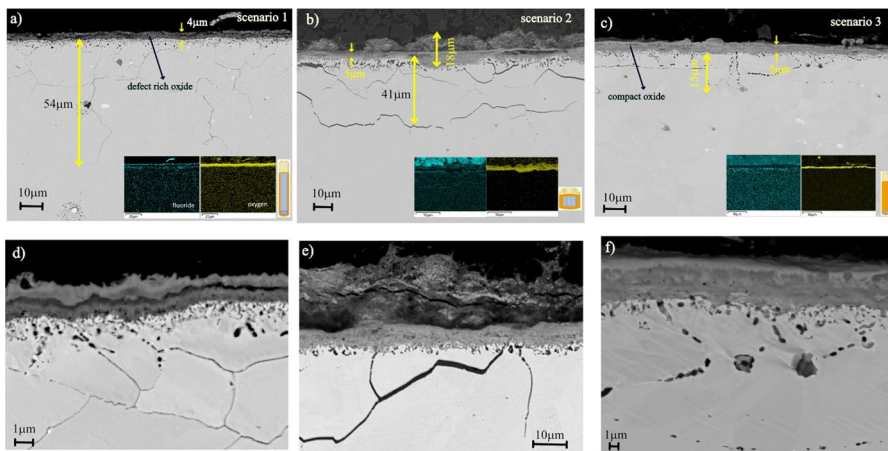


Fig. 2 Backscattered electron images of Inconel 625 exposed to LiF at 600 °C as **a** scenario 1, **b** scenario 2, **c** scenario 3 and **d**, **e**, **f** higher magnification of the oxide scales formed, respectively, on coupons 1, 2 and 3

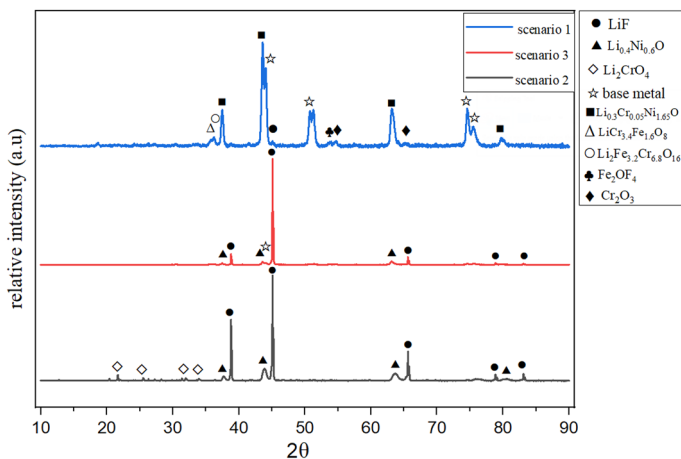


Fig. 3 XRD patterns of coupon 1 (the hottest section of the temperature gradient sample), coupon 2 (isothermal exposure in the tube furnace) and coupon 3 (isothermal exposure in vertical setup)

As shown in Fig. 2c and f, the depth of corrosion attack in coupon 3 (15 μm) has reached only one-third of that observed for coupon 1 (54 μm), and the fluoride ingress into the intergranular attack is shallow as well. This is in line with the shape of the oxide scale. A compact, 5- μm -thick oxide scale has been formed on coupon 3, which seems to be more protective against fluoride attack. The thickness of the oxide scale is quite similar for coupons 1 and 3 with limited accessibility of oxygen.

The XRD results in Fig. 3 for the oxide scale in scenario 3, which had limited access to oxygen in the vertical furnace, confirm only the participation of Ni. This phenomenon can be attributed to the lack of transport of alloying elements to the oxide scale. Since the fluoride ingress in coupon 3 was not deep into the grain boundaries and only stayed underneath the oxide scale, no increased transport of alloying elements to the oxide scale which is formed of $\text{Li}_{0.4}\text{Ni}_{0.6}\text{O}$ was detected. Since the oxygen activity in the vertical setup was assumed to be low, the oxidation of Cr to Cr(VI) ions was not possible.

After the SEM/EDX analyses, it appears clear that all three scenarios resulted in two distinct reservoirs of fluoride accumulation beneath the metal–oxide interface. The first reservoir accumulates within the Cr, Nb and Fe depletion zone beneath the oxide scale while the second distinct observation of fluoride occurred in the form of decorated grain boundaries reaching deep into the alloy. The extent and depth of this intergranular attack varied between the three scenarios. Scenario 1, which is the sample cut at the hottest part from the long strip, showed the deepest intergranular attack, without causing intragranular depletion within the surrounding grains. In order to investigate more about this sample, the oxide scale after 168 h is analyzed in Fig. 4 and also exposures on scenario 1 were extended to 1000 h. The backscattered electron image in Fig. 4 together with the EDX maps for the thermal gradient sample (scenario 1) of alloy Inconel 625 at 600 $^{\circ}\text{C}$ shows voids which have been formed underneath the oxide scale. These internal voids are due to the formation

of volatile halides (in this case, Cr/Fe and Nb fluorides), which provide the means for the metal ions to be transported away from the metal [11]. Fluoride species fill the cavities which are formed underneath the oxide scale. These fluoride pockets are formed within the same layer where chromium and niobium have been depleted, and the alloy composition is richer in nickel. It is also evident from the maps that fluoride ingress happens through the grain boundaries and reaches deeper this way. The EDX maps in Fig. 4 show a layered structure for the oxide scale on coupon 1 after 168 h of exposure. A comparison between EDX maps and the XRD spectra in Fig. 3 for scenario 1 allows for the correlation of oxides scales with lithium constituents. As shown in Fig. 4, Cr and Fe are overlapping in some parts in the oxide scale, which leads to the formation of lithiated species of Cr-Fe spinel. The Ni-rich (only 5 percent Cr) lithium nickel oxide formed on top of the oxide layers, above the Cr-Fe spinel. Interestingly, an iron and fluoride layer has formed, positioned just in between the nickel-rich scale on top and the chromium-rich scale beneath. The crystal lattice matching best is an iron oxyfluoride species Fe_2OF_4 . As shown in Fig. 3, oxygen did not follow fluoride deeper into the alloy.

These results were compared with the ones from 1000-h exposure in scenario 1. As shown in Fig. 5a, which shows the sample with the temperature gradient (scenario 1) after 1000 h, the depth of corrosion attack has tripled in comparison with the sample after 168 h of exposure. Also, the corrosion attack has affected more grains close to the surface. This intergranular attack has become finer below 50 μm . Figure 5b presents the EDX mapping which was done on the top part of the sample to see the behavior of each element after the exposure. It is apparent from the EDX maps that fluoride has reached the deeper grain boundaries, while oxygen has stayed on top. A line EDX scan was done through the first four grains beneath the oxide–metal interface of the sample in order to find out how different elements behave inside the grains and at the grain boundaries. By taking a look at the line scans in Fig. 5c, a depletion zone is noticed beneath the oxide scale for Cr, Fe and Nb. These elements are the same as those which are clearly indicated in the oxide scales shown in Fig. 4. This pattern follows along with fluoride, meaning that when fluoride gets down into the alloy microstructure along the grain boundaries, these elements are transported preferentially toward the metal–oxide interface.

As indicated in the line scan in Fig. 5c, depletion profiles for scenario 1 reach as deep as 80 μm into the alloy after 1000 h. While the intergranular attack by fluorides is progressing significantly deeper, the grains' interiors are not chemically attenuated after reaching four grains beneath the oxide scale. Where the line passes

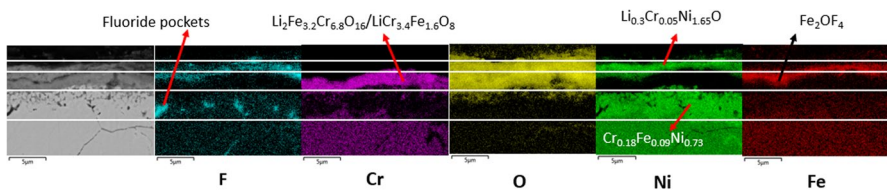


Fig. 4 BSE image and EDX elemental maps of coupon 3, phase identification has been done by matching EDX mapping data with XRD data in Fig. 3

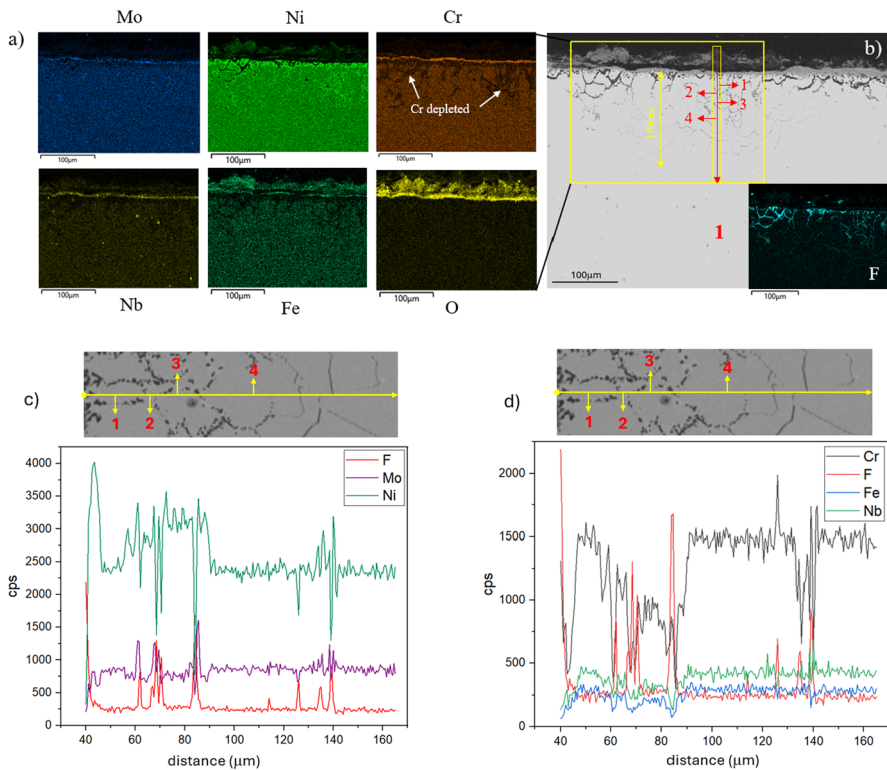


Fig. 5 a, b Cross-section BSE image of the gradient Inconel 625 (scenario 1) at the 600 °C exposure, after 1000 h in contact to LiF and c, d one line scan separated into two images for the top grains beneath the oxide scale. The first line scan part shows Ni, Mo and F, and the second line scan part shows Cr, Fe, Nb and F illustrating depleting elements

through the smaller grains like grains 1 and 2 in Fig. 5c and where the line scan has been close to the grain boundaries like grain 3, the drop in the counts indicates local depletion. This is while the counts per second for Fe, Nb and Cr have recovered to nominal values in and beyond the fourth grain, where the line scan is located further from the grain boundaries.

It is recognizable in Fig. 5d, that Cr, Nb and Fe are depleted around the grain boundaries where fluoride has access. In this line scan, the further we go from the grain boundaries (more pronounced in bigger grains like grains 1 and 4 which are marked both in Fig. 5b and d) Cr, Fe and Nb counts spike, and once the line reaches the grain boundary, the counts per second fall. However, the fluctuation noticed for Mo which are reported in Fig. 5c, shows mostly enrichment in the grain boundaries, where fluoride has reached. This reiterates that fluoride was more passive toward Mo and Ni and did not react to them at the grain boundaries. As a result, it can be said that according to the line scans, Cr, Fe and Nb contributed to the oxide scale which is lithiated. According to the EDX maps, fluoride has formed pockets underneath the oxide scale and permeated deeper into the alloy through the grain boundaries.

Considering the line scans in Fig. 5c, it can be inferred that permeating fluoride reacts with Cr, Fe and Nb in grain boundaries and delivers them to the reduced oxygen at the metal–oxide interface forming a layered structure oxide scale.

Discussion

In terms of oxygen availability, scenario 1 was similar to the isothermal sample in the vertical setup (scenario 3). However, coupon 1 was part of a strip, which, in turn, facilitates electron conductivity. In the case of the thermal gradient sample (scenario 1), the corrosion mechanism can be discussed via separating anodic and cathodic active reservoirs. In a relevant literature reference conducted in oxygen-free molten salt [12], a temperature gradient in the melt caused a difference in corrosion potentials, meaning that galvanic corrosion can happen in this case. This means that the hottest part of the sample is associated with a dominant anode reaction driving increasing amounts of fluoride into the alloy microstructure. In our case here, the drive by a thermal gradient is significantly increased by the presence of a large outer cathode.

The size of the outer cathode, which is the surface area, plays an important role. The strip sample is reaching from the hottest area far into the cold area, allowing for a much higher amount of electrons from the inner anode being allocated to oxygen reduction at the outer cathode (R 1-3.x in Table 2). Thus, despite being colder, the ongoing oxygen reduction on the surface facilitates the deep ingress of fluoride at the hot inner anode. A mechanism is suggested in Fig. 6. It is worth mentioning that the melting point of LiF is 848 °C, and at 600 °C, LiF is solid. It is apparent that at the beginning of the exposure, when LiF is not compact, oxygen can permeate through the porosities of the salt to the metal–salt interface.

In this process, oxygen reduction activates the LiF salt, lithium oxide is formed on top, while fluoride diffuses downwards through the grain boundaries and facilitates the migration of the newly available cationic species up to the metal–oxide interface. Table 2 shows the reactions and exemplary phases which are spontaneous or non-spontaneous in this process. The most interesting attack is caused by a continuous outer cathode process in scenario 1, driving fluoride toward an inner anode along grain boundaries, reaching significantly deeper than the depletion zone. This coupling between outer cathode and inner anode can only occur as long as the $\Delta G < 0$. Consulting R 4.x in Table 2, it becomes clear that indeed niobium, chromium and divalent iron fluoride fulfill this condition of spontaneity at 600 °C, while trivalent iron fluoride as well as molybdenum and nickel fluoride present with $\Delta G > 0$ and are thus not spontaneous.

The line scan in Fig. 5 clearly shows that fluoride delivers Cr, Nb and Fe to the oxide scale, e.g., $\text{Li}_2\text{Fe}_{3.2}\text{Cr}_{6.8}\text{O}_{16}/\text{LiCr}_{3.4}\text{Fe}_{1.6}\text{O}_8$. This depletion takes place through a diffusion process which delivers Cr, Fe and Nb up to the surface (shown in the magnification of Fig. 6d). Initial oxidation is following reactions R 1.x and in combined oxidation with LiF contact also by reactions R 2.x. Fluorides formed in R 2.x are nucleated concurrently to lithium incorporation into the oxide. These initial fluorides accumulate in fluoride pockets within the depletion zone of oxide

Table 2 Gibbs enthalpies and melting points retrieved from FactSage 7.3 for relevant reactions and compounds in Fig. 6 [13–15]

No.	Reaction	Reaction $\Delta G_{600^\circ\text{C}}$ in kJ	No.	Reaction	Reaction $\Delta G_{600^\circ\text{C}}$ in kJ	Compound	Melting point	References
	Oxidation without fluoride		R4.1	$\text{Cr} + 2\text{LiF} + 0.5\text{O}_2 \rightarrow \text{CrF}_2 + \text{Li}_2\text{O}$	-92.5	CrF_2	894 °C	[13, 14]
R1.1	$4\text{Fe} + 3\text{O}_2 \rightarrow 2\text{Fe}_2\text{O}_3$	-1188	R4.2	$\text{Cr} + 3\text{LiF} + 0.75\text{O}_2 \rightarrow \text{CrF}_3 + 1.5 \text{Li}_2\text{O}$	-101	CrF_3	1425 °C	[13, 14]
R1.2	$4\text{Cr} + 3\text{O}_2 \rightarrow 2\text{Cr}_2\text{O}_3$	-1797	R4.3	$\text{Fe} + 2\text{LiF} + 0.5\text{O}_2 \rightarrow \text{FeF}_2 + \text{Li}_2\text{O}$	-20	FeF_2	975 °C [13], 1100 °C [14]	[13, 14]
	Initial fluoride formation upon oxide formation, fluoride pockets shown in the fluoride map in Fig. 4		R4.4	$\text{Fe} + 3\text{LiF} + 0.75\text{O}_2 \rightarrow \text{FeF}_3 + 1.5 \text{Li}_2\text{O}$	+14	FeF_3	> 1000 °C (sublimation)	[13, 14]
R2.1	$3\text{Fe} + 2\text{LiF} + 2\text{O}_2 \rightarrow \text{FeF}_2 + 2\text{LiFeO}_2$	-712	R4.5	$\text{Nb} + 5\text{LiF} + 1.25\text{O}_2 \rightarrow \text{NbF}_5 + 2.5 \text{Li}_2\text{O}$	-120 (gas); -88 (liquid)	NbF_5	79 °C (234 °C boiling)	[13, 15]
R2.2	$6\text{Cr} + 2\text{LiF} + 5\text{O}_2 \rightarrow \text{CrF}_2 + 2 \text{Cr}_2\text{O}_3 + \text{Li}_2\text{CrO}_4$	-2501	R4.6	$\text{Ni} + 2\text{LiF} + 0.5\text{O}_2 \rightarrow \text{NiF}_2 + \text{Li}_2\text{O}$	+81	NiF_2	1380 °C	[13, 14]
	Reactions between oxides		R4.7	$\text{Mo} + 2\text{LiF} + 0.5\text{O}_2 \rightarrow \text{MoF}_2 + \text{Li}_2\text{O}$	+374	MoF_2	(gas phase only)	[13]
R3.1	$\text{Fe}_2\text{O}_3 + \text{Li}_2\text{O} \rightarrow 2\text{LiFeO}_2$	-97	R4.8	$\text{Mo} + 3\text{LiF} + 0.75\text{O}_2 \rightarrow \text{MoF}_3 + 1.5 \text{Li}_2\text{O}$	+285	MoF_3	> 600 °C (sublimation)	[13, 14]
R3.2	$\text{Cr}_2\text{O}_3 + 2\text{Li}_2\text{O} + 1.5\text{O}_2 \rightarrow 2 \text{Li}_2\text{CrO}_4$	-324	R4.9	$\text{Mo} + 5\text{LiF} + 1.25\text{O}_2 \rightarrow \text{MoF}_5 + 2.5 \text{Li}_2\text{O}$	+352	MoF_5	45 °C	[13, 14]

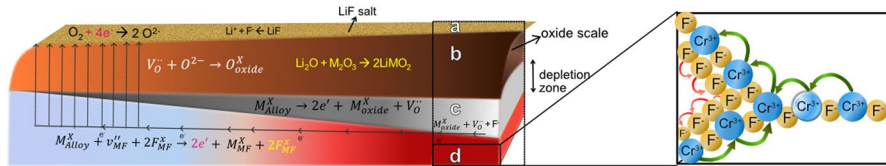


Fig. 6 Suggested mechanism for ion diffusion and electron transport along a temperature gradient and associated reactions. Left—overview over a gradient sample and right—schematic of an ion counter-stream in alloy grain boundaries

forming elements. R 2.2 actually represents a significantly higher amount of oxygen involved in the reaction, causing the formation of the $Cr(VI)$ species, lithium chromate, which was observed by significantly yellow coloring in scenario 2.

Conclusion

With this study, we could show that corrosion on alloys in contact to the alkali salt LiF and air is highly dependent on the metal component position, either along a thermal gradient and thereby an extended outer cathode surface or as an isothermally treated small sample. Furthermore, the accessibility to the oxidizing gas phase is of importance, forming the outer cathode, which effectively drives the halogen ions (here fluoride ions) into the alloy microstructure, where they combine with cations at the inner anode. Consequently, chemical plants exposed to precipitating or condensing lithium fluoride are prone to undergo rapid and deep intergranular crack formation independent of oxide scale thickness.

Three samples of Inconel 625 were analyzed in contact with lithium fluoride and filtered air in three different configurations. Coupon 2, which was exposed isothermally in the tube furnace, suffered more fluoride attack than the other two. This was associated with the degree of oxygen reduction at the surface of this sample, which activated the LiF and subsequent fluoride uptake. This claim was proved by the exposure of a similar sample in the vertical furnace with a long column of LiF on it.

Acknowledgements We want to thank Umicore, Belgium, for the financial support of this undertaking. Furthermore, we would like the head of our mechanical workshop Torbjörn Jönsson for evermore finding technical solutions for operating these challenging experiments.

Author Contributions AN built the experimental setup, conducted the corrosion exposures and performed the post-exposure analysis. Additionally, AN wrote the initial draft of the paper and incorporated the comments provided by the co-authors. BB provided the industry-related information and offered valuable comments on the draft, contributing to the refinement of the manuscript. CG performed the thermodynamic calculations and assisted with the scientific mechanisms and theories, which led to the discussion and analysis of the results. In addition, CG was actively writing on the manuscript during the whole process.

Funding Open access funding provided by Chalmers University of Technology.

Data Availability Secondary data are available on request.

Declarations

Competing Interests This research study has been financially supported by Umicore, Belgium. The authors have no financial or proprietary interests in any material discussed in this article. No conflict of interest can be declared due to the generic character of the material study.

Open Access This article is licensed under a Creative Commons Attribution 4.0 International License, which permits use, sharing, adaptation, distribution and reproduction in any medium or format, as long as you give appropriate credit to the original author(s) and the source, provide a link to the Creative Commons licence, and indicate if changes were made. The images or other third party material in this article are included in the article's Creative Commons licence, unless indicated otherwise in a credit line to the material. If material is not included in the article's Creative Commons licence and your intended use is not permitted by statutory regulation or exceeds the permitted use, you will need to obtain permission directly from the copyright holder. To view a copy of this licence, visit <http://creativecommons.org/licenses/by/4.0/>.

References

1. V. Cantatore, et al., *The Journal of Physical Chemistry C* 123, 25957 (2019).
2. H. Grabke, E. Reese, and M. Spiegel, *Corrosion Science* 37, 1023 (1995).
3. H. P. Nielsen, et al., *Progress in Energy and Combustion Science* 26, 283 (2000).
4. J. Pettersson, et al., *Oxidation of Metals* 64, 23 (2005).
5. A. Rahmel, in *Molten Salt Technology*, ed. A. Rahmel (2014), p. 265.
6. D. Williams, *Assessment of Candidate Molten Salt Coolants for the NGNP/NHI Heat-Transfer Loop* (Oak Ridge National Lab. (ORNL), Oak Ridge, TN, United States, 2006).
7. X. Wei, et al., *Applied Energy* 156, 306 (2015).
8. E. Hamdy, A. Pochi, and C. Geers, *Engineering Failure Analysis* 150, 107332 (2023).
9. B. Liu, et al., *Solar Energy Materials and Solar Cells* 170, 77 (2017).
10. B. A. Pint, et al., *Materials and Corrosion* 70, 1439 (2019).
11. P. Elliott, C. Tyreman, and R. Prescott, *Jom* 37, 20 (1985).
12. Y. Wang, C. Zeng, and W. Li, *Corrosion Science* 136, 180 (2018).
13. C. W. Bale, et al., *Calphad* 33, 295 (2009).
14. W. Haynes, *CRC Handbook of Chemistry and Physics. Edition 95* (CRC Press, Boca Raton, 2015).
15. H. Schäfer, et al., *Journal of the Less Common Metals* 9, 95 (1965).

Publisher's Note Springer Nature remains neutral with regard to jurisdictional claims in published maps and institutional affiliations.